



**Small Angle X-ray Scattering Coupled With in-situ
Electromechanical Probing of Nanoparticle-Based Resistive
Strain Gauges**

Journal:	<i>Nanoscale</i>
Manuscript ID:	NR-ART-07-2014-004129.R1
Article Type:	Paper
Date Submitted by the Author:	09-Sep-2014
Complete List of Authors:	Decorde, Nicolas; INSA, LPCNO, Sangeetha, Neralagatta; INSA, LPCNO, Genie Physique viallet, benoit; INSA, LPCNO, Genie Physique VIAU, Guillaume; Universite de Toulouse, INSA - LPCNO grisolia, jeremie; INSA, LPCNO, Genie Physique coati, alessandro; SOLEIL, vlad, alina; SOLEIL, garreau, yves; SOLEIL, Ressier, Laurence; INSA, LPCNO

Cite this: DOI: 10.1039/c0xx00000x

www.rsc.org/xxxxxx

PAPER

Small Angle X-ray Scattering Coupled With in-situ Electromechanical Probing of Nanoparticle-Based Resistive Strain Gauges

Nicolas Decorde,^a Neralagatta M. Sangeetha,^a Benoit Viallet,^a Guillaume Viau,^a Jérémie Grisolia,^a Alessandro Coati,^b Alina Vlad,^b Yves Garreau^{b,c} and Laurence Ressier ^{*a}

⁵ Received (in XXX, XXX) Xth XXXXXXXXX 20XX, Accepted Xth XXXXXXXXX 20XX

DOI: 10.1039/b000000x

A comprehensive study on the electromechanical behavior of nanoparticle-based strain gauges in action, through normal incidence Small Angle X-ray Scattering and Grazing Incidence (SAXS/GISAXS) investigations is presented. The strain gauges were fabricated from arrays of colloidal gold nanoparticle (NP) wires assembled on flexible polyethylene terephthalate and polyimide substrates, by convective self-assembly. Microstructural changes (mean interparticle distance variations) within these NP wires under uniaxial stretching estimated by SAXS/GISAXS are correlated to the simultaneously measured macroscopic electrical resistance. SAXS measurements suggest a linear longitudinal extension and transversal contraction of the NP wires with applied strain (0 to ~13%). Slope of this longitudinal variation is less than unity, implying partial strain transfer from the substrate to the NP wires. The simultaneously measured electrical resistance of the strain gauges show an exponential variation within the elastic domain of the substrate deformation, consistent with electron tunnelling through the interparticle gaps. A slower variation observed within the plastic domain suggests the formation of new electronic conduction pathways. Implications of transversal contraction of the NP wires on the directional sensitivities of strain gauges are evaluated by simulating electronic conduction in models mimicking realistic NP arrangement. Loss of directionality due to transversal current flow within these NP assemblies is deduced.

20 Introduction

The unique optical and electronic properties of colloidal nanoparticles (NPs) assembled on different substrates are being exploited for various sensing applications. In particular, these systems are attractive for sensing gases,¹⁻³ (bio)molecules,⁴⁻⁸ temperature,^{9,10} mechanical deformations,¹¹⁻¹⁷ and for photodetection.¹⁸⁻²⁰

Among these, nanoparticle-based strain gauges have excited much interest during the past years. Such resistive sensors, fabricated from colloidal NPs assembled on flexible substrates by different techniques such as airbrush spraying,¹¹ layer-by-layer deposition¹² or convective self-assembly¹⁵ indeed exhibit high sensitivities owing to an exponential variation of the tunnel resistance of the NP assembly constituting the active area with strain.^{21,22} Despite their promise, studies pertaining to such sensors have so far been largely rudimentary and models describing the behavior of nanoparticle assemblies under strain have been rather simplistic. A clear understanding of the macroscopic electromechanical behavior of NP-based strain gauges calls for an evaluation of the strain induced dynamic changes at the nanometric scale. A relevant tool to make this evaluation is Small Angle X-ray Scattering (SAXS). SAXS has been previously used to monitor the self-assembling process of NPs²³⁻²⁵ or to evaluate the packing and organization of the NPs within assemblies.²⁶⁻²⁸ The interparticle distance variation in NP assemblies during elongational strain (up to 11 %) has also been studied with SAXS, using dielectric iron oxide NP assemblies as model systems.²⁹ However, the NP dynamics governing the

performance of a NP-based strain gauge remains unexplored.

In this article, we report Small Angle X-ray Scattering (SAXS) and Grazing Incidence Small Angle X-ray Scattering (GISAXS) investigations of resistive nanoparticle-based strain gauges in action, carried out to understand the key mechanisms underlying the performance of these sensors. The mean interparticle distance variations under uniaxial stretching estimated by SAXS and GISAXS are correlated to the simultaneously measured macroscopic electrical resistance of the strain gauges and the results are analyzed further, using numerical simulations of electronic conduction.

Experimental

60 Synthesis and Functionalization of 5-21 nm Sized Gold Colloidal Nanoparticles

Synthesis of 5 nm diameter tris(2,4-dimethyl-5-sulfonatophenyl)phosphine (TDSP)-stabilized gold nanoparticles was achieved by preparing citrate-stabilized NPs, followed by ligand exchange with TDSP. To 20 mL of citrate-stabilized 5 nm sized seed gold NPs synthesized as described by Jana *et al.* and aged at room temperature for 3h, TDSP (5 mg) was added and stirred slowly, overnight.³⁰ The suspension was then concentrated by evaporating the water under reduced pressure, and the particles were precipitated as a purple solid by dropwise addition of ethanol. This precipitate was collected by centrifugation and redispersed in deionized water to a final concentration of ~0.004% vol.

15 nm citrate-stabilized gold NPs were synthesized by the Turkevich-Frens method.³¹ 21 nm sized gold NPs were

synthesized by seeded growth approach using 15 nm gold NPs as seeds as reported by Ziegler *et al.*, using HAuCl_4 as the gold source and a reductant solution consisting of citrate and ascorbic acid.³²

All these NPs were subjected to ligand exchange by refluxing them with TDSP (5–8 mg), overnight. The TDSP protected gold NPs were then concentrated by centrifugation and stirred once again with an additional quantity of TDSP (2–3 mg) for 2 to 3 h at room temperature to ensure complete exchange of the surface ligands. Subsequently, the suspensions were diluted 10 times with deionized water and re-concentrated by centrifugation, to get rid of excess ligand. This was eventually diluted with deionized water to a final concentration of $\sim 0.004\%$ vol. Mean sizes of the three types of NPs determined by Transmission Electron Microscopy (TEM) after ligand exchange were 5.1 ± 0.9 nm, 15.2 ± 1.4 nm and 21.0 ± 1.1 nm (Fig. S1, ESI).

Strain Gauge Fabrication

The flexible substrates used for fabricating the gauges were 125 μm thick Dupont polyethylene terephthalate (PET) Melinex O films and 50 μm thick Dupont Polyimide (PI) Kapton 200HN films. Before depositing the NPs, the polymer films were briefly cleaned with acetone, rinsed with water, and dried under nitrogen flow and rendered hydrophilic by exposing them to UV ozone for 5 min. NP wires were assembled on these two types of substrates using a homemade Convective Self-Assembly (CSA) setup consisting of a rectangular glass blade inclined at an angle of 20° over the horizontal substrate fixed to a temperature-regulated copper plate. This set-up was mounted under an optical microscope for real-time observations. NP assembly was carried out in Stop&Go mode (SG-CSA)¹⁵ at ambient temperature (22 – 23 $^\circ\text{C}$) and relative humidity (47 – 56%). Typically, this involved translating a 25 μL droplet of the gold colloidal suspensions wedged between the glass blade and the substrate, at a speed $v = 50$ $\mu\text{m} \cdot \text{s}^{-1}$, and dwelling for 20–30 s at chosen intervals (50 to 120 μm). The substrate temperature was maintained at 25 $^\circ\text{C}$ for 5 and 15 nm NPs and at 22 $^\circ\text{C}$ for 21 nm NPs. Note that different dwelling times and substrate temperatures were required to obtain NP wires of similar morphological characteristics from different sized NPs. The active area of the strain gauges made on PET substrates consisted of 100, 30, and 50 wire units, respectively, for the gold NPs of sizes 5, 15 and 21 nm. The active area of the strain gauges made on PI substrates consisted of 60 NP wires of 15 nm gold NPs. The NP wires constituting the active area of the strain gauges were connected between two 50 nm thick gold electrodes, 60 μm apart, fabricated by stencil lithography.

Electromechanical Tests and Small Angle X-ray Scattering Characterizations

A Deben Microtest tensile unit was used to perform uniaxial stretching of the NP-based strain gauges while simultaneously measuring the force and the strain.

For each applied strain along the x axis, Small Angle X-ray Scattering with normal incidence (along the z axis) (SAXS) and Grazing Incidence Small Angle X-ray Scattering (along the y axis) (GISAXS) were performed on the NP wires constituting the active area of the strain gauges (Fig. 1). The SAXS and GISAXS

measurements were performed at the Surfaces and Interfaces X-ray Scattering (SIXS) beamline at the SOLEIL synchrotron (Saint Aubin, France) using an X-ray beam of wavelength 0.97 \AA . The beam size was 0.2×0.02 mm^2 , three times smaller than the inter electrode distance. This allowed us to easily align the beam on the active area of the strain gauges between the two electrodes in the SAXS/GISAXS configuration. The horizontal divergence of the X-ray beam on the samples was 60 μrad . It should be noted that GISAXS measurements probed many more wires than SAXS measurements. Consequently, SAXS along the z axis gave less intense signals compared to GISAXS because of lower quantity of NPs interacting with the incident beam. The scattered beam patterns were collected for 30–90 s using the X-ray CCD detector (MARccd SX-165, 79.5 $\mu\text{m}/\text{pixel}$, 16.3 cm diameter) placed at a distance of 185.5 cm from the strain gauges. These short integration times prevent beam damage of the NP wires or the substrate. GISAXS measurements were performed with an incidence angle of 2 mrad.

The electrical resistance variation of the strain gauges, ΔR , was measured between the two electrodes connecting the NP wires, with a Keithley 6430 source meter at a constant voltage of 1 V, in synchrony with the mechanical stretching and scattering measurements. Force, strain and resistance values were continuously recorded during the entire period of the experiment, by a homemade Labview program.

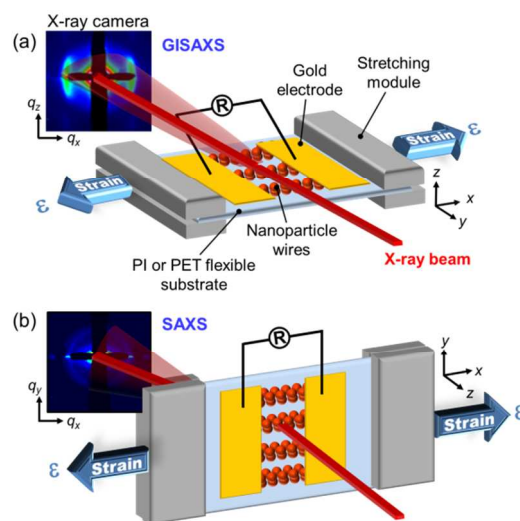


Fig. 1 Schematics of the experimental setup of small angle X-ray scattering, coupled with a stretching module and electrical resistance measurement system under (a) grazing incidence (GISAXS) and (b) normal incidence (SAXS).

Small Angle X-ray Scattering Analysis

The interaction between a transversal X-ray beam and a NP assembly gives rise to small angle scattering signal intensity $I(q)$, according to equation (1):

$$I(q) \propto P(q) \cdot S(q) \quad (1)$$

where $P(q)$ is the form factor, $S(q)$ a structure factor and q the scattering wave vector.

The form factor describes the morphology of the NPs and depends on the shape, size, and polydispersity of the NPs. The

structure factor describes the scattering contribution due to interacting NPs and depends on the distance between the NPs and their organization. When a correlation is observed between the NPs, the structure factor does not remain constant, but varies with the scattering vector; this is the Fourier transform of correlation function of NP positions.

GISAXS patterns were background corrected by subtracting the signal corresponding to the native substrate. Horizontal sections (5 pixels thick) of the patterns were integrated at $q_z = \pm 0.05 \text{ nm}^{-1}$. Each of the curves was fitted with a Gaussian function to extract the position of the maximum intensity peak along the x axis (called $q_{x \text{ max}}$) and its full width at half maximum (FWHM, called δq_x). SAXS patterns were analyzed by integrating fixed 3° angle sections from the center of the pattern between $\theta = 0^\circ$ and $\theta = 360^\circ$. A linear background was subtracted from each resulting profile and then fitted with a Gaussian function to evaluate the position of the maximum intensity as a function of the angle θ (called $q_{\text{max}}(\theta)$) and the associated FWHM δq . For each pattern, the position of the maximum intensity peak along the x axis (called $q_{x \text{ max}}$) and the y axis (called $q_{y \text{ max}}$) were estimated by fitting $q_{\text{max}}(\theta)$ with equation (2):

$$q_{\text{max}}(\theta) = \sqrt{q_{x \text{ max}}^2 \cos(\theta)^2 + q_{y \text{ max}}^2 \sin(\theta)^2} \quad (2)$$

The average NP center-to-center distances, d_x along the x axis and d_y along the y axis were estimated from the positions of the maximum intensity peak, $q_{x \text{ max}}$ along the x axis and $q_{y \text{ max}}$ along the y axis respectively, according to equation (3):

$$d_i = \frac{2\pi}{q_{i \text{ max}}} \quad (3)$$

with $i = x$ or y .

The FWHMs of the maximum intensity peak, δq_x along the x axis, allow calculation of the correlation lengths A_x along the x axis reflecting the short-range order along the NP wires:

$$A_x = \frac{2\pi}{\delta q_x} \quad (4)$$

Results and discussion

Microstructural characterization of unstrained gauges

According to our previous study in which strain gauge performance was studied as a function of NP size, strain gauges derived from 15 nm sized tris(2,4-dimethyl-5-sulfonatophenyl)phosphine (TDSP) protected gold NPs was identified to yield the best compromise between sensitivity and robustness²² and these were selected as the model system for a preliminary study. Typical design and structural characteristics of one such strain gauge are shown in Fig. 2. The optical microscopy image of part of the active area of the strain gauge displayed in Fig. 2a shows parallel micrometer wide wires of self-assembled 15 nm TDSP coated gold NPs on PET substrate, between two gold electrodes, $\sim 60 \mu\text{m}$ apart. On the atomic force microscopy (AFM) image (Fig. 2b), representative width (10 μm)

and height (60 nm) of the NP wires are shown. The scanning electron microscopy (SEM) image (Fig. 2c) presents typical NP organization of the topmost layer of the wires, where the NPs present a rather disordered hexagonal packing arrangement. The other strain gauges studied, based on 5 nm and 21 nm TDSP protected gold NPs had similar morphological characteristics (Fig. S2, ESI).

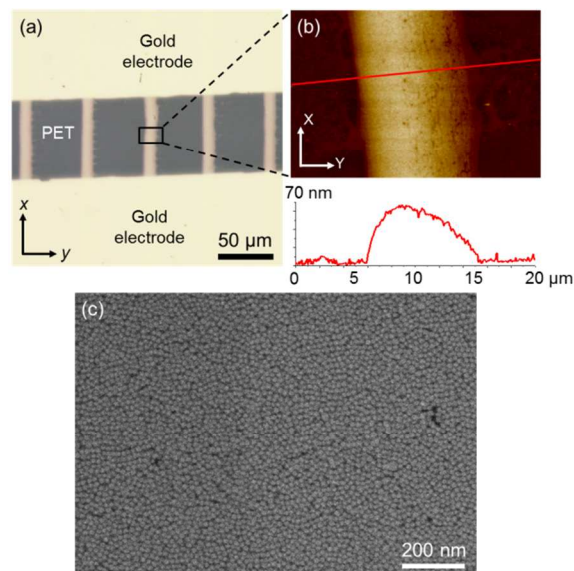


Fig. 2 (a) Optical microscopy image of the active area of a typical strain gauge based on parallel wires of 15 nm gold NPs on PET substrate, connected between two gold electrodes, (b) Top-view AFM image and associated cross-section of part of a typical NP wire and (c) SEM image showing the NP organization of the topmost layer of the NP wires. Note that the strain gauges based on 15 nm gold NPs on PI substrate have similar morphological characteristics.

The organization of the NPs within the wires constituting the active area of the strain gauges was evaluated by synchrotron X-ray scattering, both under grazing (GISAXS) and normal incidence (SAXS) (Fig. 1). Typical GISAXS and SAXS scattering patterns of unstrained gauges consisting of 15 nm gold NP wires on PET and PI substrates are displayed in Fig. 3.

The patterns are crescent shaped in grazing incidence (Fig. 3a,b) and circular in normal incidence (Fig. 3d,e). On the GISAXS patterns, a single correlation signal in the x direction is observed for PET substrate, while additional signals in the x direction and out of plane correlation spots are observed for PI substrate. While the horizontal spots may be attributed to lateral organization of the NPs within the wires (x axis), the elongated vertical spots indicate organizational order along the thickness (~ 5 NP layers) of the NP wires (z axis). A complete analysis of the GISAXS pattern is beyond the scope of this article and here we will focus only on the analysis of the position of the first correlation peak along the x axis in GISAXS and in the (x, y) plane in SAXS. The position of the maximum scattering intensity peak ($q_{x \text{ max}}$) can be clearly identified in the profiles of the patterns along the x axis, as shown in Fig. 3c and 3f for grazing and normal incidences, respectively.

Cite this: DOI: 10.1039/c0xx00000x

www.rsc.org/xxxxxx

PAPER

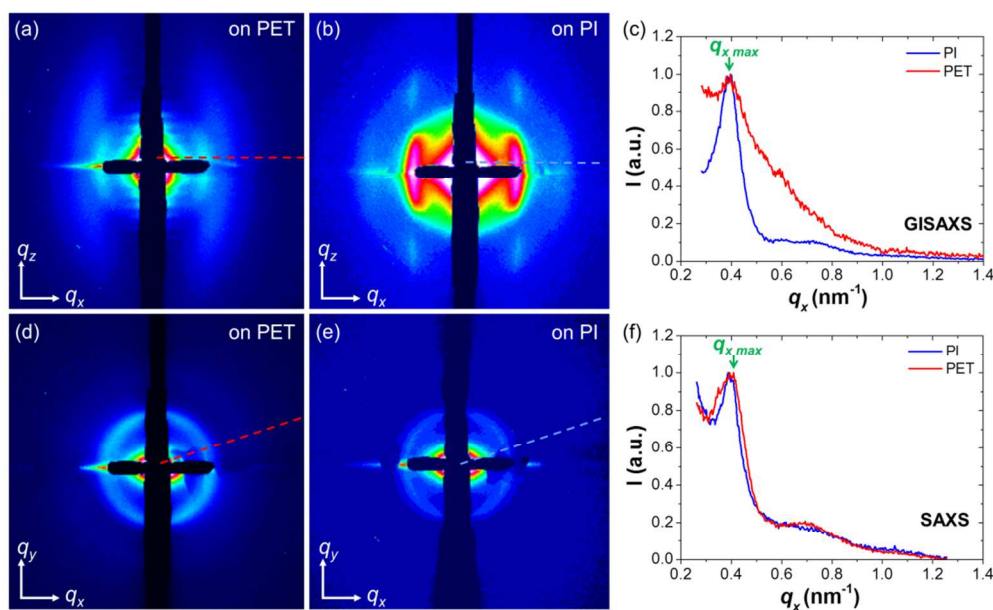


Fig. 3 Typical GISAXS (a,b) and SAXS (d,e) scattering patterns for unstrained gauges fabricated with 15 nm gold NPs assembled on PET (a,d) and PI (b,e) substrates, and GISAXS (c) and SAXS (f) profiles along the dashed lines, extracted from the scattering patterns (a,b) and (d,e), respectively.

Table 1. Parameters extracted from the scattering patterns of unstrained gauges of 15 nm gold NPs presented in Fig. 3.

Scattering Configuration	Substrate	$q_{x \max}$ [nm^{-1}]	d_x [nm]	δq_x [nm^{-1}]	Λ_x [nm]	$q_{y \max}$ [nm^{-1}]	d_y [nm]
GISAXS	PET	0.401	15.7	0.082	77	--	--
GISAXS	PI	0.401	15.7	0.046	137	--	--
SAXS	PET	0.403	15.6	0.045	140	0.403	15.6
SAXS	PI	0.403	15.6	0.03	209	0.403	15.6

Comparison of the scattering patterns from unstrained strain gauges on PET and PI substrates indicates that the substrate scattering feature overlaps with the NP scattering pattern, in case of PET. This undesirable overlapping gives rise to a higher signal to noise ratio and hence less precise measurements for experiments made on strain gauges on PET.

For both substrates, the position of the maximum intensity along the x axis determined from grazing incidence scattering is $q_{x \max} = 0.401 \text{ nm}^{-1}$, which corresponds to a center-to-center NP distance d_x of 15.7 nm. This value is in good agreement with the NP size ($15.2 \pm 1.4 \text{ nm}$) estimated by Transmission Electron Microscopy (TEM) and an interparticle distance dictated by the TDSP ligands protecting the NPs.³³

In the circular pattern obtained for normal incidence, the

horizontal and vertical distances measured from the center of the picture give the NP center-to-center distance along the traction axis x (d_x) and the transverse axis y (d_y), respectively. For unstrained gauges, both distances are the same ($d_x = d_y = d_0$), indicating an isotropic organization of the NPs within the wires. The distance d_0 (15.6 nm) measured by SAXS for gold NPs assembled on both substrates is very close to that measured in grazing incidence (15.7 nm) (Table 1).

For PI substrates, the FWHMs of the most intense peak extracted from GISAXS and SAXS profiles are 0.046 nm^{-1} and 0.03 nm^{-1} , respectively, yielding correlation lengths $\Lambda_x = 137$ and 209 nm , respectively (Table 1). The scattering peaks from similar NP wires on PET substrates show larger widths of 0.082 nm^{-1} and 0.045 nm^{-1} . The resulting correlation lengths, $\Lambda_x = 77 \text{ nm}$ and 140

nm indicate a better NP organization on PI substrates than on PET substrates.

Mechanical behavior of the NP strain gauges under stretching

For a 15 nm NP-based strain gauge on PI substrate, Fig. 4 compares the dependence of the position of the maximum intensity peak, q_{max} as a function of the angle θ from the center of the SAXS circular pattern, at rest and a high strain of 12.4%. The x axis corresponds to $\theta = 0^\circ$ and $\theta = 180^\circ$. The profiles suggest that the isotropic NP assembly within the NP wires constituting the active area of the unstrained gauges becomes anisotropic when the substrate is elongated.

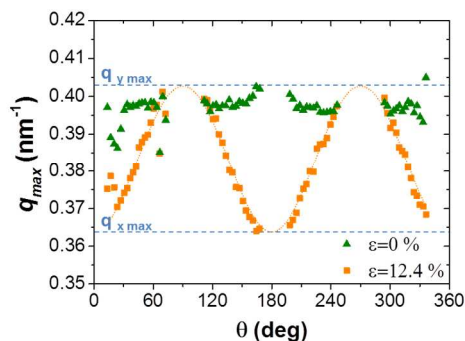


Fig. 4 Positions of the intensity maxima, q_{max} as a function of the central angle θ of the SAXS circular pattern of a strain gauge made of 15 nm NPs on PI substrate at rest (green triangles), and under a stretching strain of 12.4% (orange squares).

In order to understand the dynamics of the NPs within the wires under elongation, the relative changes in the center-to-center distance of the NPs along the x and y axes were analyzed as a function of the relative elongation (or strain) ε of the substrate, along the x axis, under normal incidence. Fig. 5 displays the plots of relative center-to-center distance variations $\Delta d/d_0 = (d-d_0)/d_0$ along the x (red disks) and y (green squares) axes, upon stretching the strain gauges of 15 nm NPs on PET and PI substrates along the x axis. Evolution of the macroscopic force applied to the gauges with the strain for each case is also plotted on the top panel (black triangles). For an elongation of either of the two substrates (PET or PI) supporting the strain gauges along the x axis, between 0 to ~13% strain, a linear increase in the relative center-to-center distance along the x axis, d_x (red disks) is observed. This strain range comprises both elastic (0–3% for PET and 0–2% for PI) and plastic (> 3% for PET and > 2% for PI) regimes of substrate deformation. Interestingly, this increase in d_x (in the longitudinal direction) is accompanied by a linear decrease in the distance along the y axis (transverse direction), d_y (green squares). This suggests a monotonous change in the interparticle distances along the two axes, albeit in opposing directions. Siffalovic *et al.* reported a linear increase of the inter-particle distance along the stretching axis and no deformation along the transverse axis for 6 nm iron oxide NP assemblies on PI substrate, a behavior different from the one observed here.²⁹ Slopes of the linear fits remain same both in the elastic and plastic regimes of the substrates (the two domains are distinguished by dotted lines on Fig. 5a and 5b), suggesting a uniform transmission of strain from the substrate to the NP wires,

irrespective of the magnitude of deformation. The slopes of the linear fits for the variation along the y axis are -0.18 and -0.20 for PET and PI substrates, respectively, approximately one third of the slopes in the stretching direction (+0.45 and +0.75 respectively, for PET and PI substrates). These ratios may very well be correlated to the Poisson's ratios of the substrates, 0.4 for PET and 0.3 for PI. The decreasing center-to-center NP distance along the transverse direction can thus be attributed to stretching-induced transversal contraction of the substrates, due to Poisson's effect. Note that the minimum possible interparticle distance will be reached along the contracting y axis at a certain value of strain, beyond which the interparticle distance d_y would saturate. This can be noticed as a slight dampening of d_y variation at strain values beyond 9% (Fig. 5).

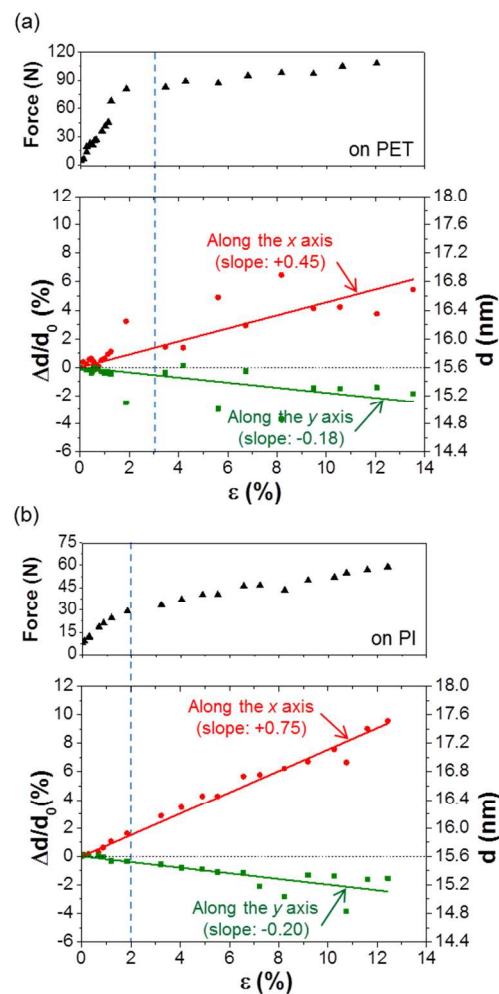


Fig. 5 Evolution of the macroscopic force applied to strain gauges and the corresponding relative NP center-to-center distance along the x axis, $\Delta d_x/d_0$ and the y axis, $\Delta d_y/d_0$ (the actual distances d_x and d_y can be read on the right axis), with respect to the applied strain ε along the x axis, for gauges based on 15 nm gold NPs on (a) PET and (b) PI substrates, measured by SAXS.

GISAXS gave results similar to that of SAXS along the x axis: a linear variation of the relative NP displacement with the applied strain. For the strain gauges based on 15 nm gold NPs assembled on PET and PI substrates, slopes of +0.51 and +0.80,

respectively, are obtained for the stretching direction, x axis (Fig. S3, ESI).

Typically, for an ideal NP-based strain gauge, a slope of 1 should be observed for the center-to-center distance variation with strain.

Inferior slopes of +0.45 and +0.75 measured in SAXS experiments (Fig. 5) for the strain gauges imply that the NP wires experience only 45% and 75%, respectively, of the strain applied to the PET and PI substrates supporting them. Note that similar slopes were obtained for duplicate gauges.

Furthermore, the GISAXS/SAXS correlation lengths of the NP wires on PET and PI substrates did not change during the entire cycle of substrate elongation. For example, the correlation length of the NP wires on PI substrate remained constant (~137 nm) right up to the substrate breakage at ~13% (Fig. S4, ESI). This suggests that the overall organization of the NP wires is conserved during the entire strain cycle. When considered in conjunction with partial strain transmission from the substrate to the NP wires suggested by the slopes inferior to 1 (Fig. 5), one might imagine strain-induced anomalous NP displacement within the wires.

This was confirmed by SEM investigations, which indicated the formation of nanoscale cracks running perpendicular to the stretching axis. Fig. 6 shows a representative SEM image of the NP arrangement within the active area of a 15 nm NP-based strain gauge on PI substrate, which had been stretched up to ~13% during SAXS measurements. The mean distance between two adjacent cracks is about 500 nm, much larger than the coherence length of the nanoparticle wires or the experimentally investigated length scales. Hence the cracks could not be distinguished by SAXS investigations and therefore do not decrease the correlation length.

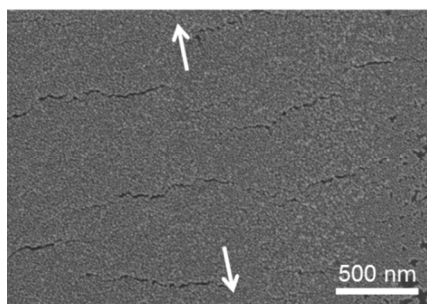


Fig. 6 SEM image of the typical NP arrangement within the active area of a 15 nm NP-based strain gauge on PI substrate after SAXS measurements. The strain gauge was subjected to stepwise strain up to a magnitude of ~13%, in the direction indicated by the white arrows.

Furthermore, the non-ideal slopes for the interparticle distance variation with applied strain reflect the imbalance between the particle-particle interactions and the particle-substrate interactions. When the particle-substrate interactions are weaker than the particle-particle interactions, NPs are likely to slide on the substrate, upon its stretching. This sliding can lead to formation of cracks, as observed for the NP assembly on PET stretched to large strains. The cracks may very well be originating from the weakest points (large defects) in the NP assembly. The substantial difference in the slope for the two substrates indicates that the NP-substrate interactions are weaker for PET substrate (greater loss of transmission), as compared to PI.

To summarize, the results obtained indicate that the changes occurring within the NP wires upon stretching include a combination of uniform relative displacement of the NPs within the assembly and other anomalous deformations such as formation of cracks. It may be supposed that cracks lead to interconnected NP islands and the NPs within these islands undergo uniform relative displacement, which leads to the observed linearity of the relative displacement with respect to strain. It should be noted that SAXS however does not yield any clues with respect to the onset of these microscopic cracks during the stretching cycle.

Electro-mechanical characterization of the strain gauges

We attempted to clarify the electrical conduction mechanism within the NP wires constituting the active area of the NP strain gauges, by simultaneously measuring both the variation of the center-to-center NP distance by GISAXS and the electrical resistance of the strain gauges under strain (0 to ~13%), comprising both elastic and plastic deformation domains of the substrate. Note that only the elastic domain is the operating range of these strain gauges and the electrical response in the plastic domain has no relevance to a typical strain gauge device performance. The study however includes the plastic domain, as it yields valuable information to better understand the mechanical behavior of the NP wires.

Typical results obtained for strain gauges of 5, 15, and 21 nm gold NPs on PET are presented in Fig. 7. A linear increase in the center-to-center NP distance variation along the x axis, with strain applied along the same axis is observed for the three gauges. The estimated slopes are close to that measured in SAXS for the 15 nm NP strain gauges (Fig. 5a). Despite the linear variation of the inter-particle distance over both the elastic ($0 < \varepsilon < 3\%$) and plastic regimes ($\varepsilon > 3\%$) of the substrate, the simultaneously measured electrical resistance shows a clear difference between the two regimes. The resistance increases exponentially within the elastic deformation regime of the substrate according to equation (5):^{14,21}

$$\frac{\Delta R}{R_0} = e^{g\varepsilon} - 1 \quad (5)$$

where the constant g illustrates the sensitivity of the gauge. Thus, the electronic conduction within the technologically relevant elastic domain is consistent with the electron tunnelling mechanism. The experimental sensitivities extracted for gauges of 5, 15 and 21 nm sized NPs are 5, 25 and, 36, respectively. Evidently, the sensitivity of the strain gauges increases progressively with the NP size, in good agreement with our previous studies.²² The magnitudes of the values are however slightly lower compared to earlier studies. It is reasonable to attribute this discrepancy to the stepwise stretching of the gauges over longer time scales than that used habitually to estimate their sensitivities, a necessary condition to carry out X-ray scattering measurements in parallel to electrical ones. Interestingly, beyond the elastic limit of the substrate, the resistance of the strain gauges starts to deviate from exponential behavior. In the plastic deformation regime of the substrate, the resistance continues to increase at a slower rate and eventually reaches a saturation point before starting to decrease, as observed for strain gauges of 15

and 21 nm gold NPs. Noteworthy is the shift in the maxima of the relative resistance variation curve to higher strain values with increasing NP size: the maxima for resistance variation is not reached even until 13% strain for 5 nm sized NPs, whereas it is reached at 8% and 7% strain respectively, for 15 and 21 nm sized particles. This is owing to increased soft component (the ligands) within the assemblies of smaller NPs.

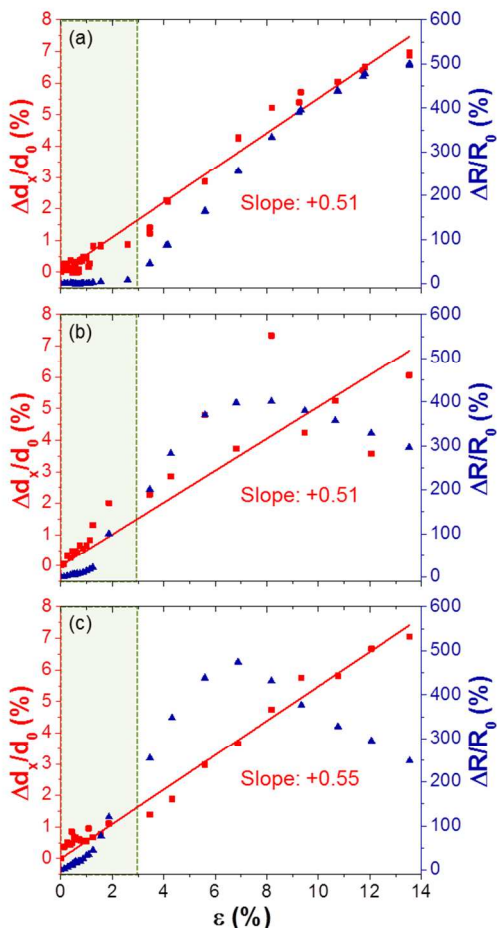


Fig. 7 Evolution of the relative NP center-to-center distance ($\Delta d_x/d_0$) measured in GISAXS and relative electrical resistance variation ($\Delta R/R_0$) of the strain gauges with respect to the applied strain, for (a) 5 nm, (b) 15 nm and, (c) 21 nm gold NPs on PET substrates. The green colored zones in the plots correspond to the elastic domain of substrate deformation (*i.e.*, the operating domain of the NP-based strain gauges).

The anomalous variation in resistance in the plastic deformation regime produced no counterpart signature in GISAXS experiments: the mean inter-particle distance increased monotonously even for large deformations. It should therefore be counter-intuitively attributed to anomalous deformations (such as formation of cracks), which went undetected by scattering experiments, but were clearly noticed in SEM images (Fig. 6). It may be supposed that the formation of cracks can trigger infilling of gaps in the bottom layers by NPs from the top layers. These effects when combined with the transversal contraction of the assembly, which confines the NPs along the transverse axis, could significantly modify the conduction pathways inside the nanoparticle assembly. In other words, new conduction pathways

could be formed, leading to electrical response anomalies, including a decrease in resistance under high strains.

Simulations on electronic conduction in nanoparticle wires

In order to estimate the consequences of the inter-particle variations along the y axis (Δd_y , perpendicular to the traction) with strain observed by SAXS (Fig. 5), on the electrical resistance of NP-based gauges, the electrical conduction within the NP wires was modelled using a home-made routine on Scilab. For this, 900 nm \times 500 nm hexagonally-packed monolayered assembly of gold NPs with a mean diameter of 15 nm and a size dispersion of 10%, separated from each other by a distance of 0.8 nm at zero strain was constructed as a mimic of the actual arrangement of the NPs within the experimentally studied 15 nm NP wire assemblies (Fig. S5a, ESI). This NP array was connected between two electrodes, one connected to the ground, the other to a voltage $V_{cc} = 1$ V. Each NP i , defined by a given position (x_i , y_i) and diameter D_i , was considered as a node of a network of resistors R_{ij} (Fig. S5b, ESI). An ideal regular square-packed assembly of 15 nm NPs (with no size dispersion) was also generated for comparison.

The resistance between the nodes i and j was computed following equation (6), where β is the tunnel decay constant, l_{ij} is the distance between the surfaces of the NPs i and j , and C a constant.

$$R_{ij} = Ce^{\beta l_{ij}} \quad (6)$$

For this simulation, C was fixed to 1 since we are only concerned with the relative resistance variation and not the absolute resistance value. β value was chosen to be equal to 6 nm⁻¹, by correcting the β value estimated in a previous work for the currently observed ineffective strain transmission using a factor $s = 0.51$ (corresponding to the experimental slope from Fig. 7b).²¹ The voltage at each node of the NP assembly was computed by resolving equation (7), where V is the vector representing the voltage at each node, I the injected current vector with $I_{i=0} = 1$ and $I_{i \neq 0} = 0$ and, G the conductance matrix.

$$[I] = [G][V] \quad (7)$$

The non-diagonal term G_{ij} of the matrix G is the opposite of the conductance between nodes i and j , and the diagonal term G_{ii} is the sum of all the conductances of the resistors connected to the node i . The macroscopic resistance R of the whole NP assembly was then computed.

For the realistic unstrained disordered hexagonal NP arrangement, the simulations indicate that the current does not flow straightforwardly from one electrode to the other but has a longitudinal (along the x axis) and a transversal component (along the y axis). This transversal current was quantified at 40%. As expected, no such effect is observed for the ideal square-packed NP assembly, with all the current being directed along the x axis.

The stretching of the simulated NP assembly was computed by modifying the position (x_i , y_i) of the NP i according to the strain ϵ , the Poisson's coefficient of the PET substrate, $\nu = 0.4$ and the experimentally measured strain transmission factor $s = 0.43$, using relation (8):

$$(x_i, y_i) \rightarrow (x_i(1+s.\varepsilon), y_i(1-v.s.\varepsilon)) \quad (8)$$

The corresponding resistance of the whole simulated NP assembly was then calculated for strains ranging from 0 to 3% (elastic domain of PET, corresponding to the working domain of strain gauges), in order to plot simulated curves of relative resistance variation measured between the electrodes (*i.e.* along the x axis) versus strain for 15 nm NP-based strain gauges on PET substrate.

Fig. 8 presents the results of this simulation for realistic hexagonal and ideal square arrangement of NPs, and for strains applied along the x axis (experimental case) and the y axis. Table 2 gives the associated sensitivities g_x and g_y obtained by fitting these simulated curves with equation (5). Note that g_x is nothing but the sensitivity 'g' measured experimentally, where the resistance relative variation is measured along the same axis as the applied strain (*i.e.*, x axis).

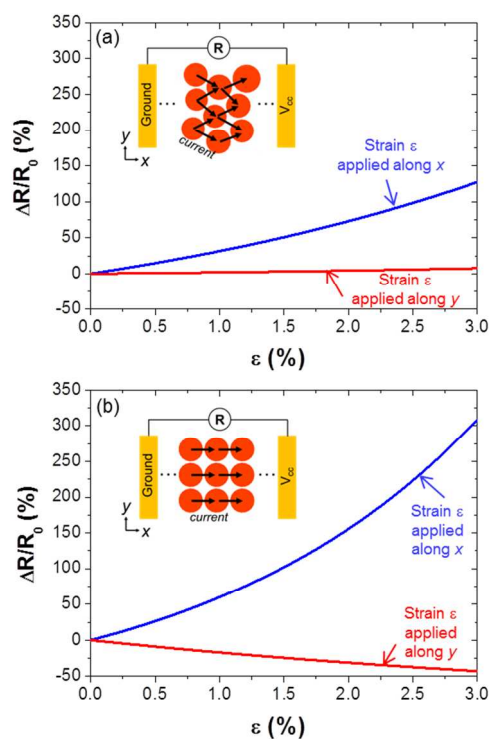


Fig. 8 Simulated relative variation of resistance of (a) a realistic hexagonal and (b) an ideal square-packed assembly of 15 nm gold NPs on PET substrate, for strain applied along the x (blue curves) and y (red curves) axis. Diagrams in the inset depict the electron flow pathways for each NP arrangement.

The simulated curves show an exponential increase in the relative resistance of the NP assembly measured between the electrodes with the strain applied along the x axis, for both hexagonal and square NP arrangement. This correlates very well with the experimental response of the hexagonally organized NP assembly. A sensitivity g_x of 27 is obtained for the realistic hexagonal NP array (Table 2). This simulated sensitivity is comparable to that estimated experimentally. The ideal square NP array shows a comparatively higher sensitivity of 47 (Table 2). The inferior sensitivity evidenced for the realistic hexagonal NP array is a direct consequence of the transversal current flowing in

the hexagonal-packed NP assembly, which is further enhanced by the decrease of inter-particle distance along the y axis upon stretching, due to transversal contraction resulting from Poisson's effect.

Moreover, these simulations also clearly show that the relative resistance variation of the NP assembly measured between the electrodes increases exponentially when the strain is applied along the y axis, in the case of realistic hexagonal NP arrangement. An opposite tendency is observed in the case of ideal square NP arrangement. A sensitivity g_y (for the strain applied the y axis and relative resistance variation measured along the x axis) of +2 is obtained for the realistic hexagonal NP array against a value of -19 calculated for an ideal square one (Table 2). That is, the NP-based gauges are sensitive not only to longitudinal deformations (along the x axis) but also to transversal ones (along the y axis). This loss of directionality of the NP-based gauges, highly dependent on the NP arrangement, is a direct consequence of the transversal current flowing in the hexagonal-packed NP assembly and of the transversal distance variation between the NPs with the applied strain.

Table 2. Sensitivities obtained by fitting the simulated relative resistance variation curves presented in Fig. 8 with the electron tunneling relationship (5).

NP arrangement	g_x	g_y
Realistic hexagonal packing	27.4	2.2
Ideal square-packing	47	-18.7

Conclusion

Nanoparticle-based resistive strain gauges derived from arrays of multilayered wires of phosphine protected gold NPs of different sizes (5–21 nm) supported on PET and PI flexible substrates were probed by small angle x-ray scattering coupled with electro-mechanical tests. The objective of these experiments was to correlate the displacement of the NPs at the nanoscale to the observed macroscopic variation of the electrical resistance of the gauges under strain.

A linear displacement of the NPs in the wires, parallel to the applied strain was observed under stretching over the entire strain regime (0 to ~13%), misleading one to believe that the strain was distributed evenly over the NP wires, while the simultaneously measured resistance of the strain gauges disproved this assumption. In fact, the electrical resistance increased exponentially within the elastic domain (0–3% for PET substrates) of the substrate deformation and varies more slowly within the plastic one. While the electric response within the elastic regime is consistent with electron tunnelling through interparticle gaps, the slower resistance increase in the plastic domain of the substrate deformation is explained by anomalous deformations within the NP wires. Comparing the strain gauges derived from two different substrates, PET and PI allowed us to identify the importance of NP adhesion to the substrate. The NP wires on PET was found to experience ~45% of the deformation applied on the substrate supporting it, while ~75% deformation

was felt by the NP wires supported on PI substrate. Importantly, transversal contraction of the NP assembly was observed by SAXS. Numerical simulations of electronic conduction indicate that this renders the NP strain gauges sensitive to transversal deformations as well, in addition to the longitudinal ones and hence loss of directional strain sensing capability. Simulations also imply a high dependence of the anisotropy of the electrical responses of NP assemblies upon their packing parameters. This anisotropy can in turn reduce the overall sensitivity of the strain gauges.

Acknowledgements

This work was supported by the French National Agency (ANR) in the frame of its program 'P2N' (NanoFlexiTouch project no ANR-12-NANO-0015-01). The authors thank Soleil for providing access to synchrotron radiation facilities (Project number 20120889).

Notes and references

²⁰ ^a Université de Toulouse, LPCNO, INSA-CNRS-UPS, 135 avenue de Rangueil, Toulouse 31077, France. Fax: +33561559697; Tel: +33561559672; E-mail: laurence.ressier@insa-toulouse.fr

^b Synchrotron SOLEIL, L'Orme des Merisiers Saint-Aubin - BP 48, Gif-sur-Yvette 91192, France.

²⁵ ^c Université Paris Diderot, Sorbonne Paris Cité, MPQ, UMR 7162 CNRS, Paris 75013, France.

† Electronic Supplementary Information (ESI) available. [TEM images and size histograms of the gold nanoparticles, AFM images of wires of 5 and 21 nm gold nanoparticles on PET substrates, evolution of the relative NP center to center distance of 15 nm gold NP-based strain gauges on PET and PI substrates with respect to applied strain, evolution of the GISAXS correlation length of 15 nm gold NP-based strain gauge on PI substrate with respect to applied strain, schematics of the electronic conduction model]. See DOI: 10.1039/b000000x/

References

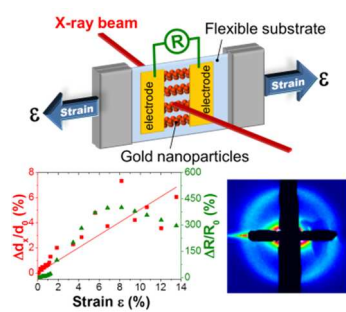
- 1 A. N. Shipway, E. Katz, and I. Willner, *ChemPhysChem*, 2000, **1**, 18–52.
- 2 F. J. Ibañez and F. P. Zamborini, *ACS Nano*, 2008, **2**, 1543–1552.
- 3 A. B. Kashyout, H. M. A. Soliman, H. Shokry Hassan, and A. M. Abousehly, *J. Nanomater.*, 2010, **2010**, 341841.
- 4 E. Katz and I. Willner, *Angew. Chem. Int. Ed.*, 2004, **43**, 6042–6108.
- 5 M. Lahav, R. Gabai, A. N. Shipway, and I. Willner, *Chem. Commun.*, 1999, 1937–1938.
- 6 A. Yu, Z. Liang, J. Cho, and F. Caruso, *Nano Lett.*, 2003, **3**, 1203–1207.
- 7 A. B. Kharitonov, A. N. Shipway, and I. Willner, *Anal. Chem.*, 1999, **71**, 5441–5443.

- 8 S. Zhang, W. Yang, Y. Niu, Y. Li, M. Zhang, and C. Sun, *Anal. Bioanal. Chem.*, 2005, **384**, 736–741.
- 9 P. Murugaraj, D. E. Mainwaring, T. Jakubov, N. E. Mora-Huertas, N. A. Khelil, and R. Siegle, *Solid State Commun.*, 2006, **137**, 422–426.
- 10 P. Murugaraj, D. Mainwaring, and N. Mora-Huertas, *J. Phys. Appl. Phys.*, 2006, **39**, 2072–2078.
- 11 J. Herrmann, K.-H. Müller, T. Reda, G. R. Baxter, B. Raguse, G. J. J. B. de Groot, R. Chai, M. Roberts, and L. Wiczorek, *Appl. Phys. Lett.*, 2007, **91**, 183105.
- 12 T. Vossmeier, C. Stolte, M. Ijeh, A. Kornowski, and H. Weller, *Adv. Funct. Mater.*, 2008, **18**, 1611–1616.
- 13 M. Segev-Bar, A. Landman, M. Nir-Shapira, G. Shuster, and H. Haick, *ACS Appl. Mater. Interfaces*, 2013, **5**, 5531–5541.
- 14 C. Farcau, H. Moreira, B. Viallet, J. Grisolia, D. Ciuculescu-Pradines, C. Amiens, and L. Ressier, *J. Phys. Chem. C*, 2011, **115**, 14494–14499.
- 15 C. Farcau, N. M. Sangeetha, H. Moreira, B. Viallet, J. Grisolia, D. Ciuculescu-Pradines, and L. Ressier, *ACS Nano*, 2011, **5**, 7137–7143.
- 16 Y. Kim, J. Zhu, B. Yeom, M. Di Prima, X. Su, J.-G. Kim, S. J. Yoo, C. Uher, and N. A. Kotov, *Nature*, 2013, **500**, 59–63.
- 17 M. Segev-Bar and H. Haick, *ACS Nano*, 2013, **7**, 8366–8378.
- 18 J. Tang, G. Konstantatos, S. Hinds, S. Myrskog, A. G. Pattantyus-Abraham, J. Clifford, and E. H. Sargent, *ACS Nano*, 2009, **3**, 331–338.
- 19 W. Yan, N. Mechau, H. Hahn, and R. Krupke, *Nanotechnology*, 2010, **21**, 115501.
- 20 B. Liu, Z. Wang, Y. Dong, Y. Zhu, Y. Gong, S. Ran, Z. Liu, J. Xu, Z. Xie, D. Chen, and G. Shen, *J. Mater. Chem.*, 2012, **22**, 9379–9384.
- 21 H. Moreira, J. Grisolia, N. M. Sangeetha, N. Decorde, C. Farcau, B. Viallet, K. Chen, G. Viau, and L. Ressier, *Nanotechnology*, 2013, **24**, 095701.
- 22 N. M. Sangeetha, N. Decorde, B. Viallet, G. Viau, and L. Ressier, *J. Phys. Chem. C*, 2013, **117**, 1935–1940.
- 23 D. Dunphy, H. Fan, X. Li, J. Wang, and C. J. Brinker, *Langmuir*, 2008, **24**, 10575–10578.
- 24 S. V. Roth, T. Autenrieth, G. Grübel, C. Riekel, M. Burghammer, R. Hengstler, L. Schulz, and P. Müller-Buschbaum, *Appl. Phys. Lett.*, 2007, **91**, 091915.
- 25 P. Siffalovic, E. Majkova, L. Chitu, M. Jergel, S. Luby, A. Satka, and S. Roth, *Phys. Rev. B*, 2007, **76**, 195432.
- 26 D. Altamura, V. Holý, D. Siliqi, I. C. Lekshmi, C. Nobile, G. Maruccio, P. D. Cozzoli, L. Fan, F. Gozzo, and C. Giannini, *Cryst. Growth Des.*, 2012, **12**, 5505–5512.
- 27 K. Bian, J. J. Choi, A. Kaushik, P. Clancy, D.-M. Smilgies, and T. Hanrath, *ACS Nano*, 2011, **5**, 2815–2823.
- 28 A. T. Heitsch, R. N. Patel, B. W. Goodfellow, D.-M. Smilgies, and B. A. Korgel, *J. Phys. Chem. C*, 2010, **114**, 14427–14432.
- 29 P. Siffalovic, L. Chitu, K. Vegso, E. Majkova, M. Jergel, M. Weis, S. Luby, I. Capek, J. Keckes, G. A. Maier, A. Satka, J. Perlich, and S. V. Roth, *Nanotechnology*, 2010, **21**, 385702.
- 30 N. R. Jana, L. Gearheart, and C. J. Murphy, *J. Phys. Chem. B*, 2001, **105**, 4065–4067.
- 31 J. Turkevich, P. C. Stevenson, and J. Hillier, *Discuss. Faraday Soc.*, 1951, **11**, 55–75.
- 32 C. Ziegler and A. Eychmüller, *J. Phys. Chem. C*, 2011, **115**, 4502–4506.
- 33 G. Schmid and U. Simon, *Chem. Commun.*, 2005, 697–710.

110

115

TOC



⁵ SAXS/GISAXS and electromechanical studies on gold nanoparticle-based resistive strain gauges are carried out to unravel the mechanism of deformation and the results are analyzed using simulations on electronic conduction.